UCLA
UCLA Previously Published Works

Title

Strong Ground Motion Characteristics from 2016 Central Italy Earthquake Sequence

Permalink

https://escholarship.org/uc/item/3z75j0q5

Authors

Zimmaro, Paolo
Scasserra, Giuseppe
Stewart, Jonathan P
et al.

Publication Date

2018-05-31

Supplemental Material

https://escholarship.org/uc/item/3z75j0q5#supplemental

Data Availability

The data associated with this publication are in the supplemental files.

Peer reviewed

Strong Ground Motion Characteristics from 2016 Central Italy Earthquake Sequence

Paolo Zimmaro,[a)] M.EERI, Giuseppe Scasserra,[b)] Jonathan P. Stewart,[a)] M.EERI, Tadahiro Kishida,[c)] M.EERI, Giuseppe Tropeano,[d)] Massimina Castiglia,[b)] and Panagiotis Pelekis[e)]

The central Italy earthquake sequence has, to date, generated three mainshocks: **M**6.1 24 August, **M**5.9 26 October, and **M**6.5 30 October 2016. These events, along with aftershocks, were well recorded by Italian networks, and are among the normal fault earthquakes with the highest number of recordings globally. We process records for six events using NGA/PEER procedures. Many recording sites lacked V_{S30} assignments, which we provide using measured shear wave velocity profiles where available and a local geology proxy otherwise. Stations at close distance, including near the hanging wall, exhibit fling step in some cases but no obvious rupture directivity. The data exhibit fast anelastic attenuation at large distances (>100 km), as predicted by recent Italy-adjusted global models, but not by Italy-specific models. We partition residuals from Italy-adjusted global models, finding negative event terms at short periods (weaker than average shaking). We apply Kriging of within-event peak acceleration and velocity residuals using a global semi-variogram model to estimate the spatial distribution of peak accelerations, which are generally most intense south-west of Mt. Vettore.

INTRODUCTION

We develop a database of uniformly processed recordings from the Central Italy earthquake sequence, assign necessary metadata for analysis (source, path, and site parameters), evaluate near-fault attributes that are of special interest in highly damaged areas, and investigate attributes of the dataset relative to available global and local ground motion models.

[a)] Department of Civil and Environmental Engineering, University of California Los Angeles, CA, USA
[b)] Dipartimento di Bioscienze e Territorio, Università degli studi del Molise, Campobasso, Italy
[c)] Department of Civil Infrastructure and Environmental Engineering, Khalifa University of Science Technology and Research (KUSTAR), Abu Dhabi, UAE
[d)] Dipartimento di Ingegneria Civile, Ambientale e Architettura, Università di Cagliari, Italy
[e)] Department of Civil Engineering Educators, School of Pedagogical and Technological Education, Greece

Recordings of the 2016 event sequence, as well as major prior events in Italy, are of particular global significance for studies of normal fault ground motions. For example, in the NGA-West2 global database (Ancheta et al. 2014), 64% of recordings for normal fault events with **M**>5.5 are from Italy, a figure that will surely grow as a result of the 2016 events.

We obtained digital unprocessed recordings from the European strong motion (ESM) database (Luzi et al., 2016) for six earthquake events listed in Table 1 that occurred between 24 August and 30 October 2016. The information presented here is similar to that in reports by the Geotechnical Extreme Events Reconnaissance (GEER) association (GEER, 2016, 2017). Luzi et al. (2017) undertook similar ground motion analyses to those presented in the GEER documents and this paper, but with different data processing, source models, and site parameters to those used here, as explained below. Their interpretation of the data also differs from that presented here.

The database contains recordings from 298 stations. The majority of recordings are from two networks: (1) the Italian Accelerometric Network (Rete Accelerometrica Nazionale, RAN; ran.protezionecivile.it/, last accessed 18 September, 2017), owned by the Italian Civil Protection Department (Dipartimento della Protezione Civile, DPC), and (2) the National Seismic Network (Rete Sismica Nationale, RSN; http://www.gm.ingv.it/index.php/rete-sismica-nazionale, last accessed 18 September, 2017), owned by Istituto Nazionale di Geofisica e Vulcanologia (INGV). Data from other networks were also considered (details in Chapter 3 of GEER, 2016). RAN comprises stations located inside the former Italian National Electric Company (Ente Nazionale per l'Energia ELettrica, ENEL) transformer cabins, generally equipped with Syscom MS2007 instruments and free-field stations mostly equipped with Kinemetrics sensors (Etna, K2, Makalu, FBA23 or Episensor). General characteristics of the instruments are: 3-channel accelerometers, a full-scale range of 1g/2g, and 18-24 bit resolution. RSN instruments are generally Kinemetrics Episensor FBA-ES-T; the unit consists of three Episensor force balance accelerometer modules mounted orthogonally, with full-scale recording ranges of $\pm$ 1g to $\pm$ 2g (Luzi et al., 2016).

Events designated as mainshocks in Table 1 comprise the first significant event in the sequence for a particular portion (or segment) of the causative fault. Events designated as aftershocks are assigned as such based on spatial and temporal attributes using both: (1) a traditional approach based on time and distance windows, with the latter evaluated as the radial distance from the mainshock epicenter (Gardner and Knopoff, 1974), and (2) an approach used

in the NGA-West2 project (Bozorgnia et al., 2014) that considers the Gardner-Knopoff time window in combination with between-event distance metric CR_{JB}, defined as the distance from the centroid of the surface projection of the possible aftershock rupture surface to the surface projection of the mainshock rupture plane (Wooddell and Abrahamson, 2014). Both approaches provide similar results for the subject events. In Table 1, events classified as CL1 are either mainshocks or foreshocks, while events classified as CL2 are considered aftershocks.

Table 1 also lists the number of usable recordings for each event at the time of our analysis (September 2017). For all events, additional recordings were made available, but were either flagged as 'bad-quality' in the ESM database (which we have confirmed by inspection of unprocessed records) or as 'restricted' in the ESM database (data are not publicly available). Figures 1 and 2 show the spatial distribution of all permanent recording stations relative to the August and October event sources, respectively. The fault planes shown in these figures are as described by Galadini et al. (201x).

Table 1. Attributes of the earthquake events analyzed.

Date	$\mathbf{M}$[1]	Number of recordings	Aftershock flag[2]	Description
24 August 2016	6.1	235	CL1	Mainshock
24 August 2016	5.3	180	CL2	Aftershock
26 August 2016	4.8	132	CL2	Aftershock
26 October 2016	5.4	178	CL1	Foreshock
26 October 2016	5.9	224	CL1	Mainshock
30 October 2016	6.5	212	CL1	Mainshock

[1] Moment magnitude values from Galadini et al. (201x) and ESM database (Luzi et al., 2016).
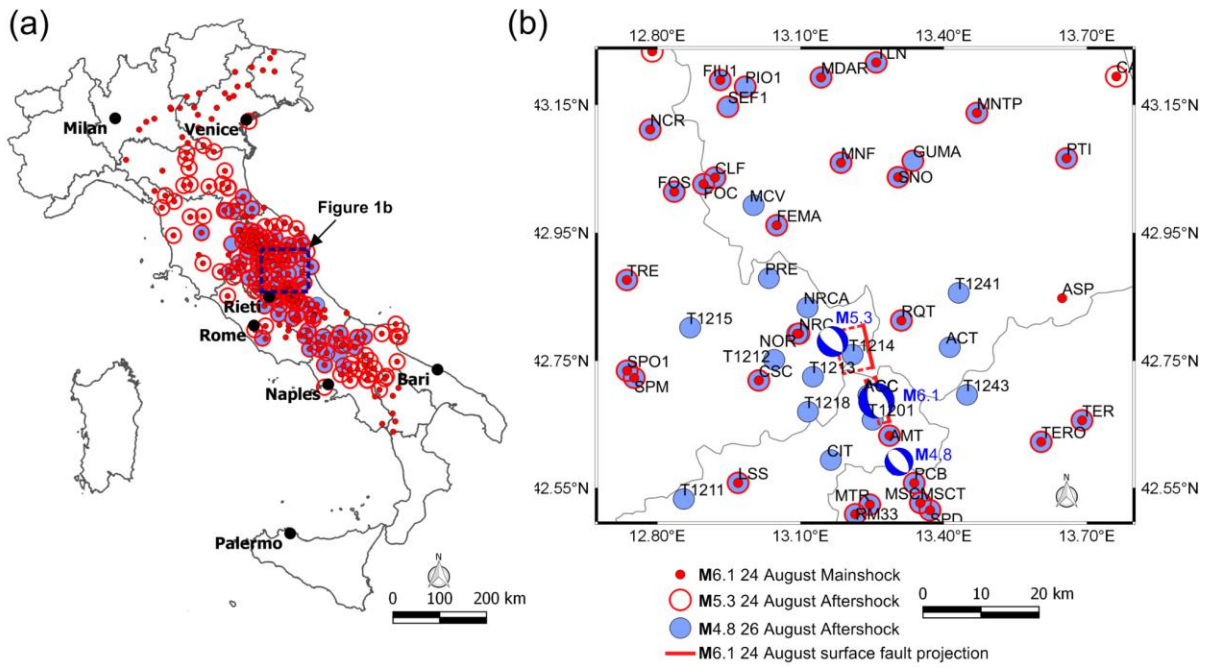[2] CL1 = mainshocks or foreshocks, CL2 = aftershocks (Wooddell and Abrahamson, 2014).

Figure 1. (a) Locations of instruments that recorded **M**6.1, **M**5.3, and **M**4.8 August 2016 events; (b) close-up view of the instruments in the epicentral area.
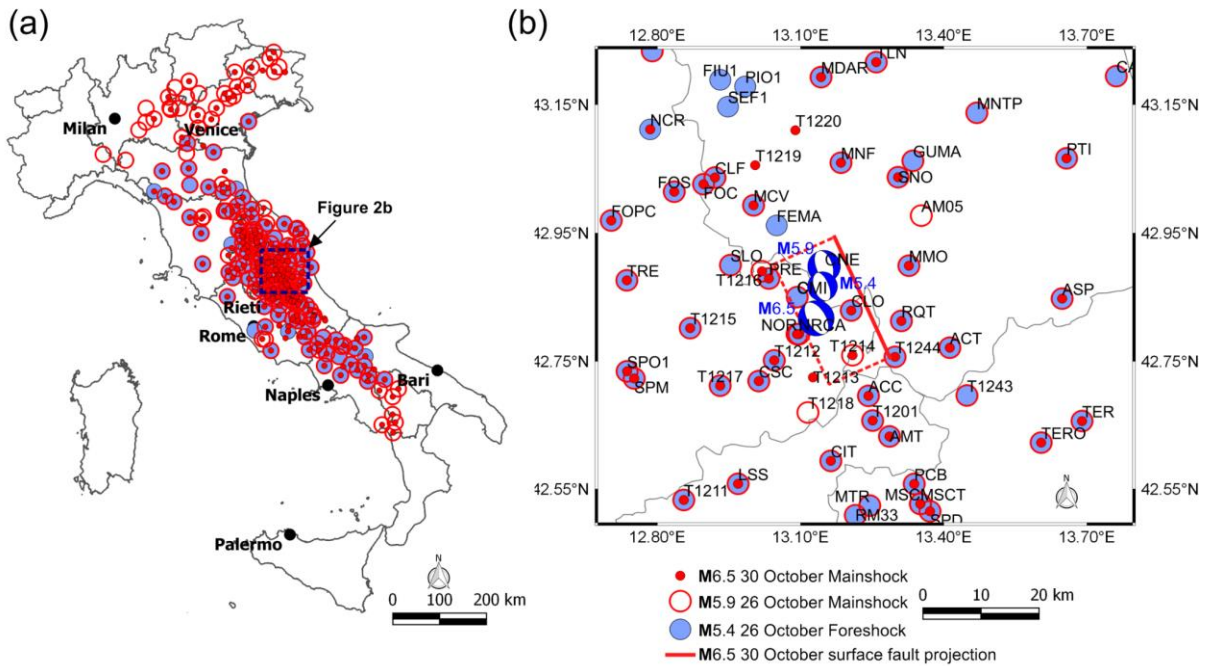

Figure 2. (a) Locations of instruments that recorded **M**6.5, **M**5.9, and **M**5.4 October 2016 events; (b) close-up view of the instruments in the epicentral area.

SITE CONDITIONS

In keeping with international standards, we use time averaged shear wave velocity in the upper 30 m (V_{S30}) as the primary site parameter. We take V_{S30} from measurements where

possible. The largest source of measured V_{S30} values for the subject region are station monographs available in the ESM database (Luzi et al., 2016). Additional measured values for recording station sites not having direct measurements in station monographs are presented by Kayen et al. (201x) and Scasserra et al. (2009a) (five sites), GEER (2017) (six sites, details below), both of which are based on spectral analysis of surface waves (SASW), and d'Onofrio et al. (2009) (one site), based on downhole tests. When measurements at the site or nearby are unavailable, we estimate V_{S30} on the basis of relationships with surface geology, which is identified using local, relatively large-scale maps (from 1:10.000 to 1:25.000 scale) available for the Umbria, Lazio, Marche, Toscana and Emilia regions. In other cases, we used available documentation from *ad-hoc* site-specific microzonation studies or technical papers (e.g. for Molise region), details on this approach are provided in GEER (2016).

V_{S30} assignments are classified in order of preference as follows (Scasserra et al. 2009a):

- Data Source Type A: On-site measurements of velocity using established geophysical techniques (downhole, cross-hole, surface wave methods, etc.).

- Type B: Velocity measurements available at nearby sites (up to 500 m) having the same surface geology as the subject station.

- Type C: Velocity estimated based on general correlation relationships between mean shear wave velocity and surface geology.

- Type D: V_{S30} estimated as the average value of the subsoil category indicated in the ESM database following the Italian Building Code (Ministry of the Infrastructures, 2008; NTC08). For categories A ($V_{S30} > 800$ m/s), B (360 m/s $< V_{S30} < 800$ m/s) and C (180 m/s $< V_{S30} < 360$ m/s), we take V_{S30} as 800, 540 and 270 m/s, respectively. This method is used for 16 stations without geophysical data or surface geologic descriptions.

Luzi et al. (2017) apply broadly similar criteria, focusing on Types A and C, using the subset of V_S profiles in the ESM database (i.e., whereas we have 52 Type A V_{S30} values across 298 sites, Luzi et al., 2017 have 30 Type A values for 230 sites).

Figure 3 shows data source type for the stations that produced recordings considered in this paper. An electronic supplement to this paper provides the main attributes of the 298 digital accelerometer stations, including location, surface geology, V_{S30}, and instrument housing type (Table S1). Among these are 15 temporary stations deployed after the **M**6.1 24 August event

(INGV working group, 2016). For Type C, we use relationships recommended by Scasserra et al. (2009a) between surface geology and V_{S30} for a number of surface geologic categories relevant to the subject regions. These include: Quaternary alluvium categories segregated by sediment depth and material texture (Qal,thin; Qal,deep; Qal,coarse), older Quaternary alluvium (Qoa), Quaternary to Tertiary alluvial deposits (QT), Tertiary sandstone formations (Tss), Pleistocene to Pliocene conglomerate (Pc), and Mesozoic limestone and volcanic rocks (Ml and Mv, respectively). For Quaternary categories, Scasserra et al. (2009a) confirmed the applicability of the relations proposed by Wills and Clahan (2006), whereas for the older bedrock units, Italy-specific relationships were developed. Table S2 (electronic supplement) compares site classifications and V_{S30} values used in this paper and those used by Luzi et al. (2017) as provided in the ESM database (Luzi et al., 2016).
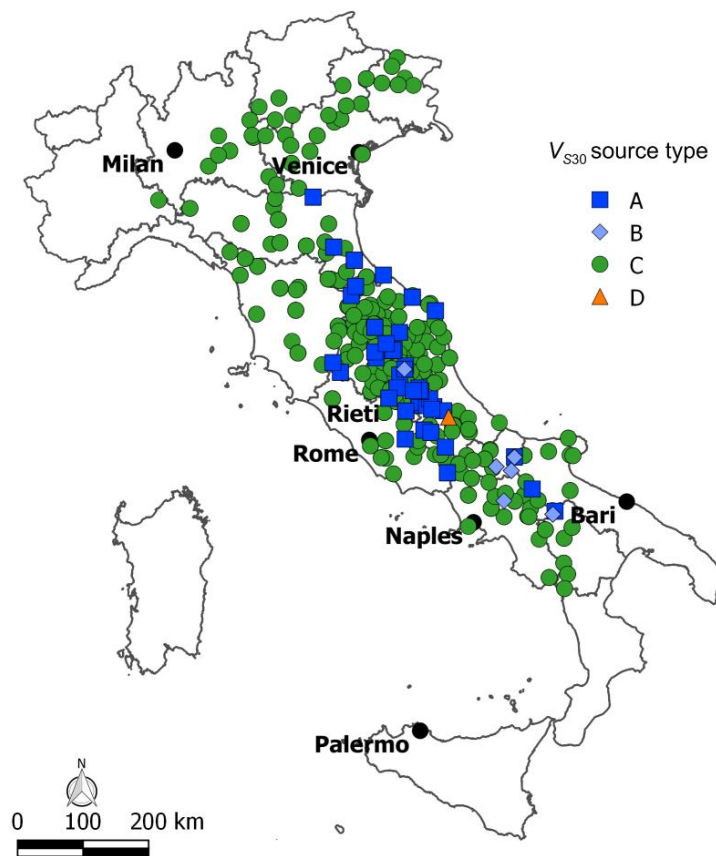

Figure 3. Data source types used for V_{S30} estimations for all considered recording stations.

During the reconnaissance activities performed after the August 2016 events, the seventh author performed SASW testing for six stations for which only Type D estimates had previously been available. As a result, the following six sites are now classified as Type A: (1) Foligno (FOC), (2) Poggio Cancelli (PCB), (3) Selle Pedicate, Campotosto (SPD), (4)

Mascioni, Campotosto (MSC), (5) Norcia (NRCA), and (6) Montereale (MTR). Table 2 lists station codes, locations, measured V_{S30} and number of recorded events (among those analyzed in this paper) of these recording station sites.

Table 2. Measured V_{S30} and details of the newly characterized recording station sites.

Station code	Lat. (deg)	Lon. (deg)	Measured V_{S30} (m)	Geology (age)	Elevation (m.a.s.l.)[1]	# of recorded events
FOC	43.02630	12.89651	285	Recent alluvial deposits (Holocene)	821	6
PCB	42.55802	13.33799	366	Marly sandstone (Miocene)	1315	6
SPD	42.51514	13.37104	521	Sandstone (Miocene)	1338	6
MSC	42.52676	13.35084	540	Sandstone (Miocene)	1335	6
NRCA	42.83355	13.11427	491	Limestone (Jurassic)	927	1
MTR	42.52402	13.24480	1130	Sandstone (Miocene)	915	5

[1] Meters above sea level.

DATA PROCESSING

The ESM database has both unprocessed and processed accelerograms (using the ITalian ACcelerometric Archive, ITACA – INGV procedure; Pacor et al. 2011). We downloaded unprocessed records, which were processed using Pacific Earthquake Engineering Research (PEER) center procedures (Ancheta et al., 2014). This processing includes applying component-specific low-pass filters and identifying the lowest usable frequency. We defined the usable bandwidth of each record in response spectral space from 100 Hz to the high-pass corner frequency multiplied by 1.25. The 1.25 factor is used applied to reduce the impact on spectral ordinates of lower frequencies where the energy in the time series is impacted by filtering. Figure 4 shows the number of available records with frequency, which indicates a range of lowest usable frequency from 0.02 to 3.6 Hz. Median-component intensity measures (RotD50) are computed from the corrected accelerograms (Boore, 2010). Luzi et al. (2017)

used corrected records from Luzi et al. (2016), which were processed using the ITACA – INGV procedure. Processing performed using PEER and ITACA protocols generally provide similar results (Boore et al., 2012).
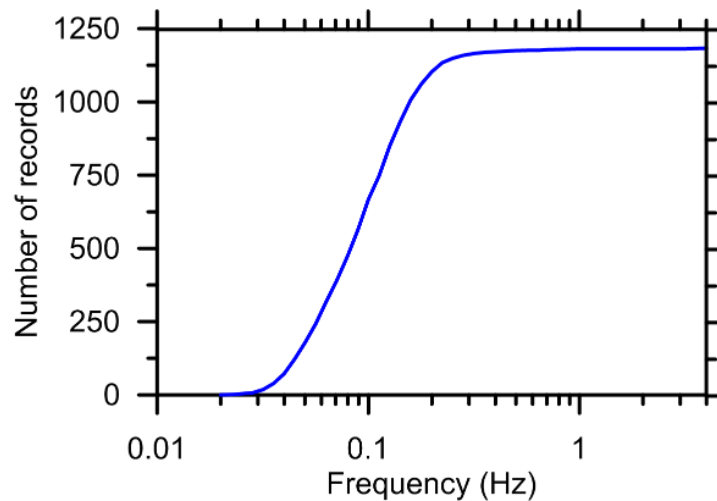

Figure 4. Number of available records with frequency for the processed records.

Special processing was applied to selected near-fault records to preserve fling step displacements (i.e. static ground displacements, resulting from fault rupture; Kamai et al. 2014), as described in the next section. For each record, metadata are assigned for earthquake source (seismic moment, moment magnitude, rake angle, strike, dip, finite fault models for mainshocks), path (rupture distance and distance to surface projection of fault for mainshocks, hypocenter distance and epicentral distance for aftershocks), and site parameter V_{S30} (previous section). Finite fault models and other source characteristics used for mainshocks are as given in Galadini et al. (201x) and are based on inversion procedures utilizing both geodetic and ground motion data. All analyses shown in this paper are performed using trimmed finite fault models. Luzi et al. (2017) used earlier, apparently untrimmed finite fault models by Tinti et al. (2016) and Chiaraluce et al. (2017), which generally provide smaller site-to-source distances, and thus slightly larger predictions of intensity measures from ground motion models.

As would be expected in any large accelerometer network, some instruments did not record properly one or more earthquake events during the period 24 August to 30 October 2016. The NRCA station, located in Norcia, did not record any mainshocks. The NRCA station only recorded the **M**4.8 26 August aftershock. This results from a sudden power outage during the earthquakes and lack of auxiliary power. The RQT station, in Arquata del Tronto, recorded all six events. One of the components (NS) is unusable (signal is essentially zero) in five of the six recordings. The only usable three-component recording from the RQT station (in the

analyzed period) is from the **M**5.4 26 October 2016 foreshock. RQT is of special interest because it is among the few instruments located on the footwall (for all events) in the near-fault area. Data from six stations (AQA, FCC, PRE, RQT, NOR, and AMT) published on the ESM website after the 24 August 2016 mainshock, became unavailable and were flagged as 'restricted' on 11 November 2016. Following correction, those recordings were re-published on 23 December 2016. One of these updates involved the Amatrice recording (AMT) of the **M**6.1 24 August event, which reduced in amplitude by a factor of 2.0. Some published results (including Chapter 3 of GEER 2016) use the earlier, pre-correction, version of this record.

NEAR-SOURCE GROUND MOTIONS

As shown in Figures 1b and 2b, there are several recordings near the surface projections of the **M**6.1 24 August and **M**6.5 30 October mainshocks fault sources. While data from these stations were processed using standard procedures, additional processing was also performed to identify pulse-like features and to preserve static offsets, which is described here.

The **M**6.1 24 August event was recorded by three stations in the near field: AMT, NRC and NOR (Figure 1b). Figure 5 shows 5% damped pseudo-acceleration response spectra (PSA) for horizontal-component ground motions at these stations, processed using standard PEER procedures (removing static offset). A characteristic feature of near-fault ground motions with forward rupture directivity effects is polarization of shaking in the fault normal (FN) direction, particularly at long spectral periods (e.g., Somerville et al., 1997; Watson-Lamprey and Boore, 2007). To investigate this potential effect, the corrected ground motions were rotated into FN and fault parallel (FP) orientations. The Amatrice (AMT) ground motion has higher amplitudes in the FN direction at short oscillator periods (< 1.0 sec), whereas the two components are practically equivalent beyond about 0.6 sec. The NRC and NOR motions have slightly higher amplitudes in the FN direction at long periods (> 1.0 sec). Taken as a whole, the available data do not provide strong evidence for FN-polarized ground motions as would be anticipated if significant forward rupture directivity effects had occurred.
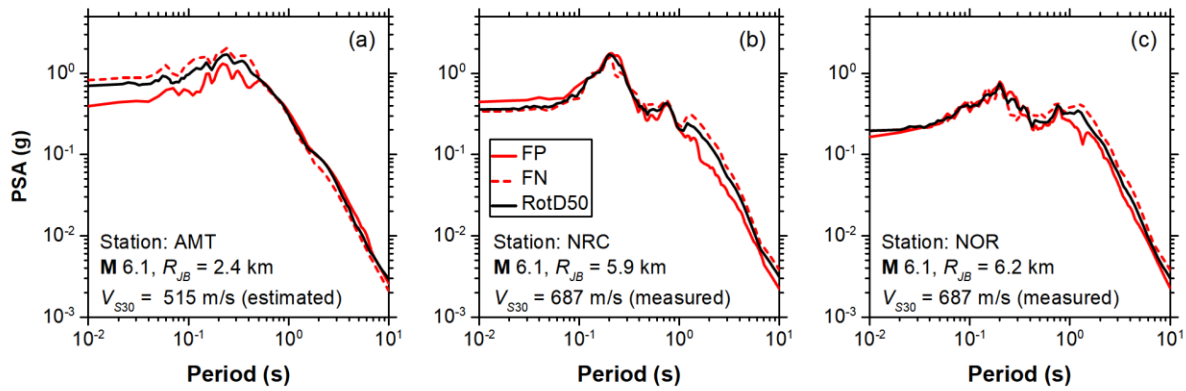
Figure 5. Pseudo-spectral acceleration response spectra (5% damping) for Amatrice (AMT) and Norcia (NRC, NOR) sites from the **M**6.1 24 August event.

The **M**6.5 30 October event was recorded by nine stations in the near field (Figure 2b). Figure 6 shows response spectra for these records, which as before were corrected using PEER processing that removes fling effects. Stations T1214, CLO, CNE are on the hanging wall and T1244 is on the footwall near the surface expression of the fault. These four stations would be the most likely to show an effect of rupture directivity, but no such effect is apparent from the comparison of FN and FP spectra (FN would be expected to be higher). The other spectra shown in Figure 6 are in locations of interest due to their proximity to villages and other features discussed elsewhere in this issue (Sextos et al., 201x; Franke et al., 201x; and Durante et al., 201x).

Aside from examination of spectra, another way to examine possible near-fault effects in ground motions is through identification of possible pulses in velocity time series (i.e. clear short-duration pulses occurring early in the velocity ground motion time series that are indicative of forward directivity or fling step effects). Using data from the 30 October event, these characteristics were checked for stations T1214, CLO, and CNE using the Shahi and Baker (2014) multi-component pulse identification procedure, with the results shown in Figure 7. Using this approach, we first defined, for each selected pair of ground motion time series, the orientation in which velocity pulses are strongest. We then calculated the pulse indicator for that orientation. Our results show that for the T1214 and CLO stations, weak pulses are present roughly in the FP orientation (300 deg azimuth, Figure 7). For the CNE station, the Shahi and Baker (2014) algorithm does not show the presence of pulses. Our results are somewhat consistent with similar analysis performed by Luzi et al. (2017), based on a single-orientation algorithm (Baker, 2007). Our interpretation, based on visual inspection of the

extracted pulses and on the quantitative analysis of the pulse indicator scores, is that, for this event, the pulse effects are weak. As shown in GEER (2016), similar analyses of near-fault records from the 24 August event do not reveal the presence of significant pulses.

Accordingly, both the ground motion polarization and pulse identification results indicate that forward rupture directivity effects are not significant in the ground motion recordings from these events. This outcome is not particularly surprising for dip-slip ruptures (Spudich et al., 2013).

We investigate the presence of fling-step effects that can be present in near-source recordings, especially on the hanging wall of dip-slip faults. As described in GEER (2016), we did not find appreciable fling in the three near-fault records from the 24 August event.

Figure 8 shows vertical displacement time series for the three hanging walls records (T1214, CLO, CNE) from the 30 October event. These records have been reprocessed using a procedure developed to preserve static (permanent or tectonic) displacements (Gregor et al., 2002). The amount of vertical-component fling-step in these records are -46, -87, and -16 cm, respectively. Station T1214 is close to (~1 km) GPS station ARQT, which recorded a vertical displacement of -45 cm, which can be compared to -46 cm from double-integration of the T1214 accelerogram. Even though we have used different data processing protocols, these results are in good agreement with similar analysis performed by Luzi et al. (2017).

Ground motion stations ACC, AMT, and T1216 (not on hanging wall) also have nearly co-located GPS stations (ACCU, AMAT, and MUVI, respectively). As shown in GEER (2017), both instrument types in each case showed a lack of fling step displacement, which is an encouraging lack of 'false positives'.

COMPARISON TO GROUND MOTION MODELS

Ground motion models (GMMs) are typically used within seismic hazard assessment frameworks for predicting expected levels of shaking given magnitude, source-to-site distance, site condition, and other factors. In this section, we compare GMM predictions to observed data. The objective of these comparisons is not to identify a preferred model. Rather, the aim is to facilitate visualization and identification of the main features of the recorded data.

In recent years, several studies focused on the selection of suitable GMMs for use in global (Stewart et al., 2015), regional (Delavaud et al, 2012), or site-specific applications in Italy (Zimmaro and Stewart, 2017). These selections are often performed by comparing GMM

predictions over a parameter space of engineering interest. While local models can reflect local geologic and tectonic conditions, which may differ from those represented by global models, the limited database size used to develop local models may be inadequate to constrain GMMs for conditions often critical for application (large magnitudes and small distances). Global models are more effective for such conditions, because they are typically based on much larger databases, but may contain bias with respect to local effects. Regional adjustment factors can be used to reduce the bias of global models, which are typically applied to anelastic attenuation and site effects.

In consideration of the above, we compare recorded data to the following GMMs applicable to shallow-crustal earthquakes in active tectonic regions: (1) an Italy-specific model by Bindi et al. (2011; hereafter Bea11), (2) the average of three NGA-West2 GMMs, without regional adjustments (Boore et al., 2014; Campbell and Bozorgnia, 2014; and Chiou and Youngs, 2014; hereafter NGA2), and (3) the average of those same three NGA-West2 models but now applying regional adjustments for Italy (NGA2-I). The Abrahamson et al. (2014) model is not applied for these comparisons due to its lack of an Italy-specific adjustment. We note that the seismic intensity measure used in the Bea11 model is the geometric mean of the horizontal components, while the NGA2 and NGA2-I models use the median-component ground motion, RotD50, as defined by Boore (2010). These two approaches for defining horizontal 'averaged' ground motions have been shown to provide similar results, both in investigations of this specific database (results not presented here for brevity) and in previous studies using different databases (Boore, 2010; Bradley and Baker, 2015; Boore and Kishida, 2017). As a result, the difference in the intensity measure definitions used in the considered models does not affect the outcomes presented in this study.
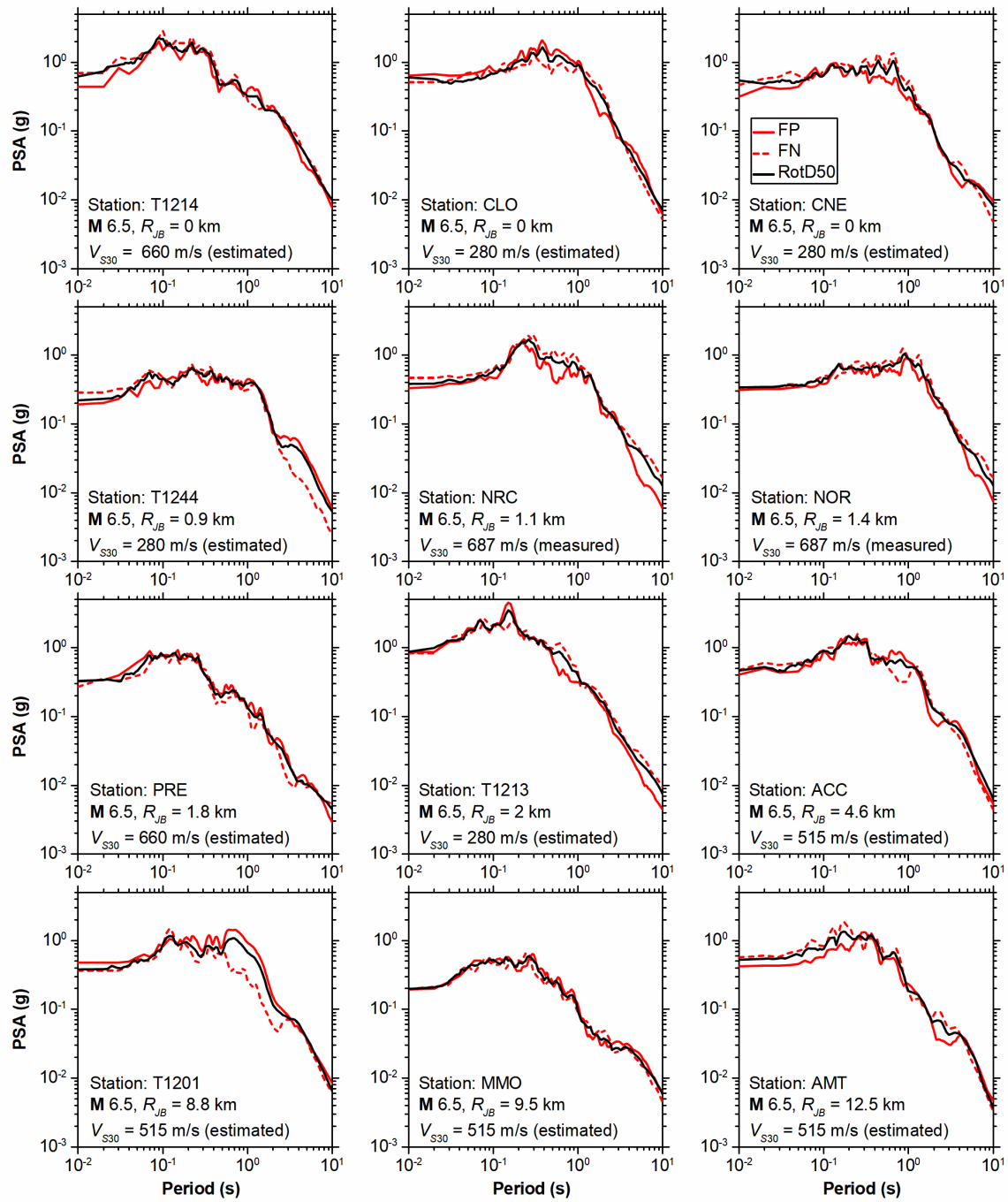
Figure 6. Pseudo-spectral acceleration response spectra (5% damping) for nine near source recording sites from the **M**6.5 30 October 2016 event.
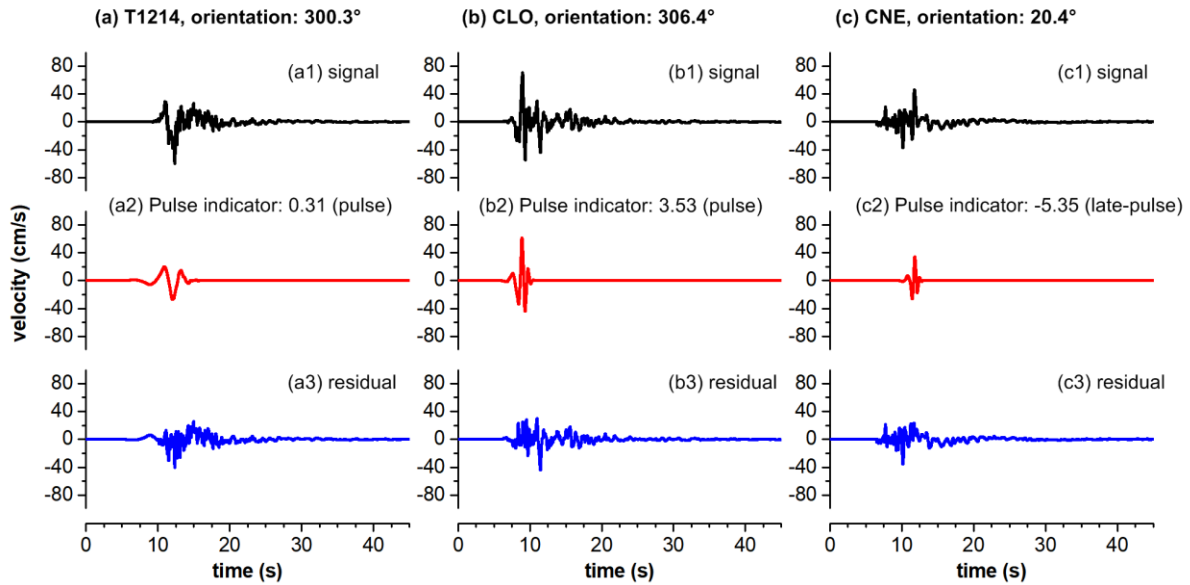
Figure 7. Original ground motion, extracted pulse, and residual ground motion for the **M**6.5 30 October 2016 event recorded at the (a) T1214, (b) CLO, and (c) CNE stations.
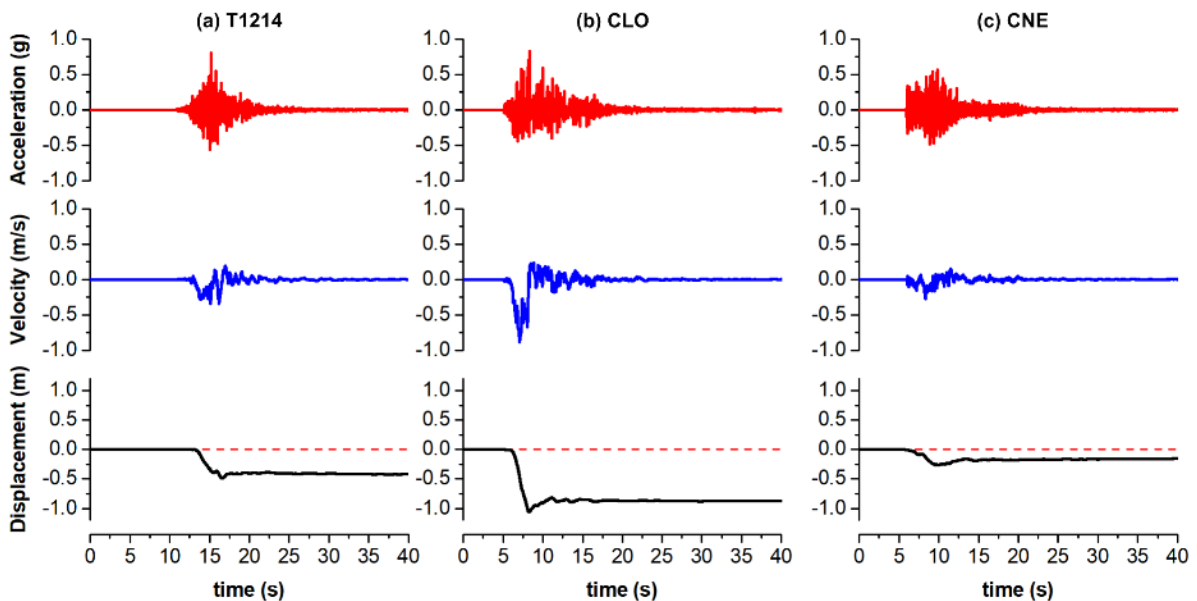

Figure 8. Vertical component of acceleration, velocity, and displacement time-series for the **M**6.5 30 October 2016 event, processed using the Gregor et al. (2002) procedure for the (a) T1214, (b) CLO, and (c) CNE stations.

The selected GMMs use different distance metrics. The Bea11 and Boore et al. (2014) models use closest distance to the surface projection of the rupture plane, or Joyner and Boore distance (R_{JB}). The Campbell and Bozorgnia (2014) and Chiou and Youngs (2014) models use the closest distance to the rupture plane (R_{RUP}). All distances are calculated using the trimmed finite-fault models for the three mainshocks (Galadini et al., 201x). We idealize the aftershocks (**M**4.8-5.4) as point sources for calculating distances.

Figures 9 and 10 show the distance-dependence of median-component peak acceleration (PGA) and velocity (PGV) for the six events in Table 1. Recorded data are plotted with different symbols for three site categories (categories A, B, and C, respectively according to NTC08): (1) rock ($V_{S30} > 800$ m/s), (2) stiff soil and weathered rock ($360 < V_{S30} < 800$ m/s), and (3) soft soil ($V_{S30} < 360$ m/s). Also shown in Figures 9 and 10 are median predictions from the Bea11 model, the average of the three NGA2, and the average of the NGA2-I models. Median predictions have been calculated using $V_{S30} = 580$ m/s. The models fit the data reasonably well for $R_{JB} = 0$-100 km. Beyond this distance, there is a relatively fast attenuation of ground motions in all six events. This feature, captured only by the NGA2-I models (with regional adjustment for Italy), is a characteristic of Italian data observed from pre-2006 data by Scasserra et al. (2009b) and from the L'Aquila event sequence by Stewart et al. (2012). At short distances (i.e. 1-10 km), data are sparse, but there are differences between models. In particular, Bea11 has a wider flat-attenuation region at close distance, likely due to the use of a larger 'finite fault dimension' term.
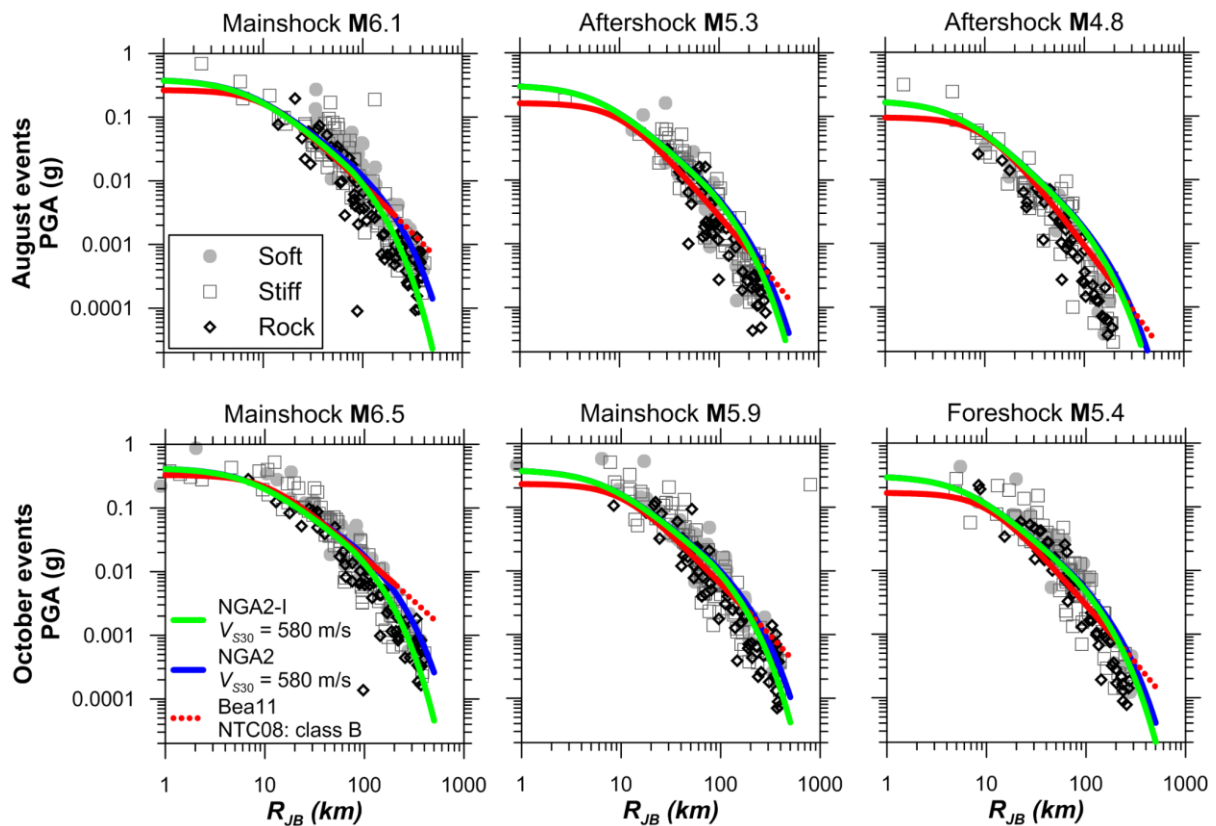

Figure 9. Variation of PGA with R_{JB} for rock (NTC08: A), stiff soil (NTC08: B), and soft soil (NTC08: C, D, E) and predictions from the selected ground motion models. For Bea11 (red lines), dotted lines indicate predictions beyond the published range of model validity.

The performance of multiple GMMs relative to the data can be more directly assessed using

residuals analysis. We calculate total residuals for each data point considering the appropriate source-to-site distance and site condition as follows:

$$R_i = \ln(Y_i) - \mu_{ln}\big(\mathbf{M}_i, R_i, V_{S30,i}\big) \tag{1}$$

where Y_i is the ground motion intensity measure from recording i and μ_{ln} is the natural log mean for that same intensity measure from a GMM, with the appropriate arguments for the model (magnitude, distance, site parameter). For the NGA-West2 models (NGA2 and NGA2-I), μ_{ln} is taken as the average of the natural log means of the three considered GMMs. For Bea11, the median prediction is used. Total residuals are then partitioned as follows to compute the random effect for each event η (also called the event term), and the remaining residual ε (also called within-event residual) (e.g., Stafford, 2012):

$$R_i = c_k + \eta + \varepsilon_i \tag{2}$$

where c_k is a bias term assumed for the present analysis to be null (to the extent that such a bias might exist, it is included in our estimates of η).
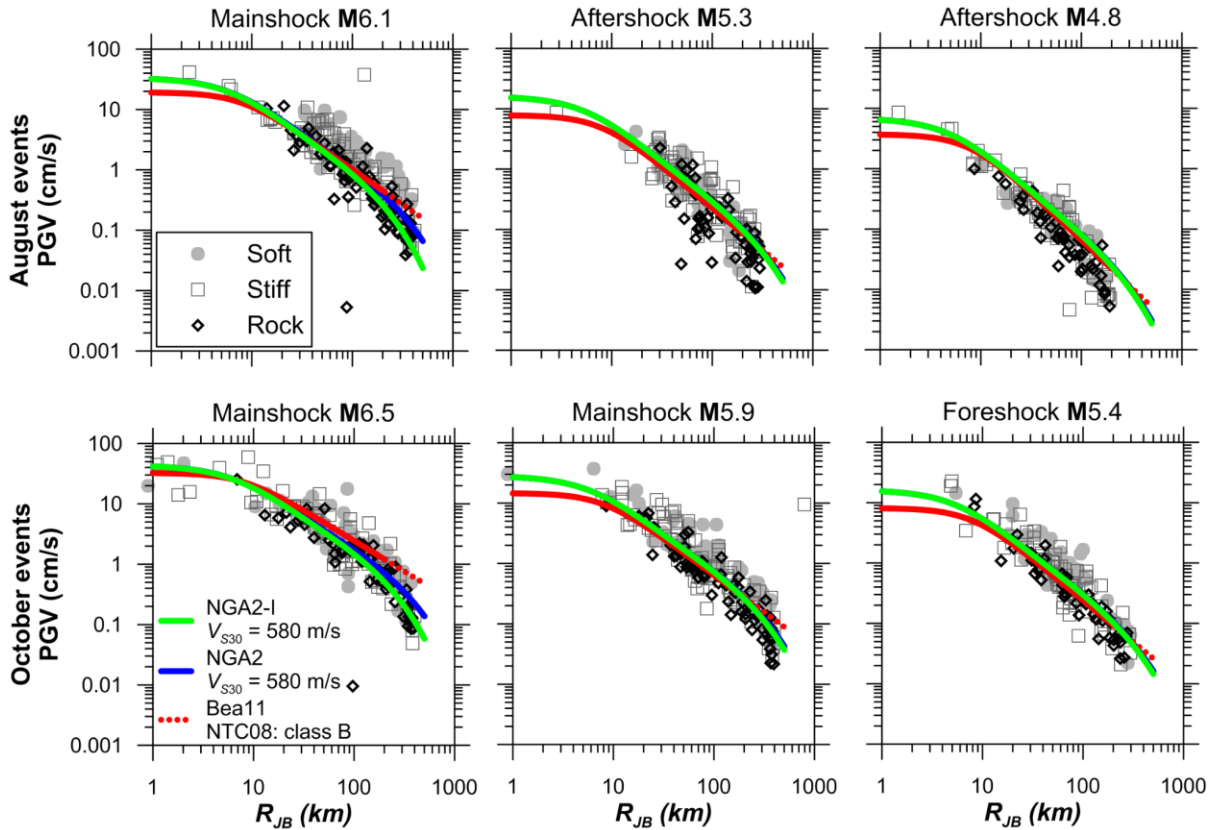

Figure 10. Variation of PGV with R_{JB} for rock (NTC08: A), stiff soil (NTC08: B), and soft soil (NTC08: C, D, E) and predictions from the selected ground motion models. For Bea11 (red lines), dotted lines indicate predictions beyond the published range of model validity.

Figures 11-13 show within-event residuals for PGA, PGV, and PSA for a 2 sec oscillator period for all six events as a function of distance. Binned means and standard deviations are shown using five bins per log-cycle (due to limited data, a single bin is used for R_{JB} = 0-10 km). The results indicate good consistency between GMMs and mainshock data up to 100 km. At large distance (> 100 km), the Bea11 residuals consistently trend downwards, indicating underprediction of anelastic attenuation in this model. For the NGA2 and NGA2-I models, the residuals trends upwards for some events and downwards for others, indicating that the anelastic attenuation is somewhat variable between events but may be reasonable in an average sense. The recommended distance range for the Bea11 model is 0-200 km. As a result, residuals for distances beyond 200 km represent model extrapolations.

The event terms are shown in Figure 14 as a function oscillator period for the six considered earthquakes. Also shown are plus/minus one between-event standard deviations from the Boore et al. (2014) and the Bindi et al. (2011) GMMs. For short periods (PGA to 0.5s), the Central Italy event terms for the NGA2-I range from zero to -1, whereas they are nearly zero for longer periods. This trend is consistent with what was observed for the 2009 L'Aquila event ground motions using NGA-West1 GMMs with an Italy adjustment (Stewart et al., 2012).

SPATIAL DISTRIBUTION OF GROUND MOTIONS

When examining the effects of earthquakes on the natural or built environment, which is the focus of several papers in this issue, it is important to consider the spatial distribution of ground shaking. For well recorded earthquakes like those in the 2016 Central Italy sequence, such ground motion distributions are invariably more complex than suggested by the smooth variation with distance provided by GMMs. Several prior studies show that these spatial distributions are best evaluated from Kriging applied to within-event residuals (ε_i in Eq. 2) in lieu of Kriging of ground motions themselves (e.g., Stafford, 2012; Kwak et al. 2012, 2016). The primary benefit of this approach is that first-order path and ergodic site effects are removed by the residuals calculation, so that the Kriged quantity is stationary. We presented an earlier version of ground motion maps derived using the processes described here in GEER (2017). Luzi et al. (2017) have previously provided ground motion maps based on direct interpolation of intensity measures from recordings.

We perform Kriging of within-event residuals (ε) for the three mainshock events using the NGA2-I GMMs. Kriging requires a semi-variogram model to guide interpolation between

observations. Semi-variogram models are subject to regional dependences (e.g. Wagener et al., 2016). However, in this study, we use the well-established global model by Jayaram and Baker (2009). Figures 15-16 show the resulting spatial distributions of ε for PGA and PGV for the **M**6.1 24 August, **M**5.9 26 October, and **M**6.5 30 October events (additional results in GEER 2017). The ε maps have the most meaning in regions with data, reverting to zero in areas without ground motion instruments (i.e., areas east of the fault rupture). Most of the regions shown in Figures 15-16 that are near instruments have positive ε, meaning that the GMM is under-predicting the ground motion. This under-prediction is most pronounced in areas off the ends of the faults to the north, northwest, and southeast. As a population, the mean of ε must be null, which is not evident in Figures 15-16 because of observations (some of which are negative ε) beyond the limits of the map.

These maps can be used to compute ground motion intensity measures for location j as:

$$\overline{\ln(Y)}_j = \mu_{\ln}\left(\mathbf{M}, R_j, V_{S30j}\right) + \eta + \varepsilon_j \tag{3}$$

where $\overline{\ln(Y)}_j$ is the mean estimate of the ground motion intensity measure for location j. As in Eq. (1), the natural log mean on the right side is taken as the average of the means from the NGA2-I models. Maps of the spatial distribution of PGA and PGV for **M**6.1 24 August, **M**5.9 26 October, and **M**6.5 30 October mainshock events are given in Figures 17-18. These maps are prepared for a uniform site condition of $V_{S30} = 580$ m/s, and as such will be biased for particular sites having different stiffnesses. The **M**6.1 24 August event is a two-segment rupture (Galadini et al., 201x). For this event the highest ground motion intensities are localized in the vicinity of the southern segment. For the 26 and 30 October events, the highest values of PGA and PGV are evident in the south-western portion of the finite fault models. The ground motions in these maps do not account for local site response effects (including topographic amplification) that appears to be significant in several damaged regions (Sextos et al., 201x).
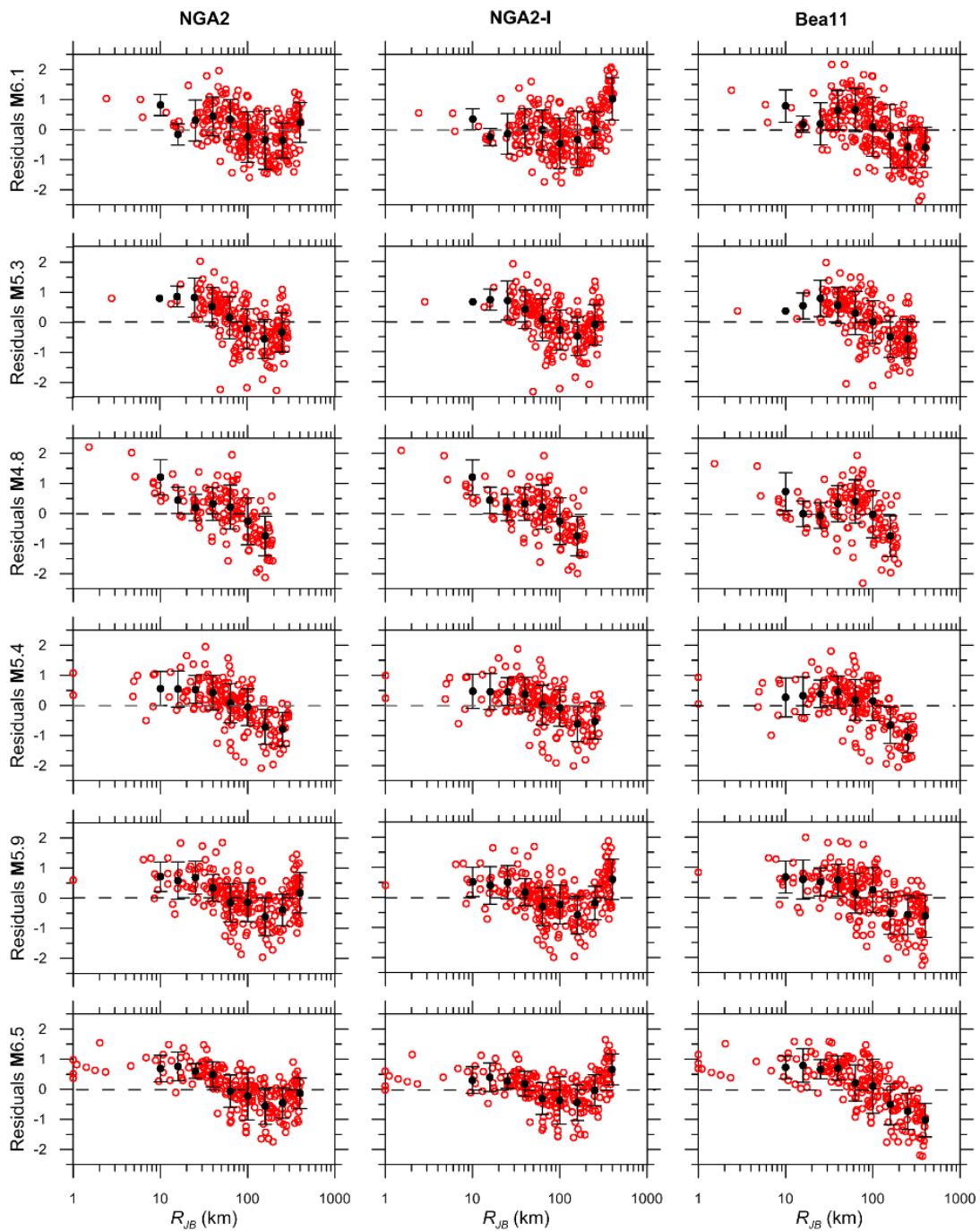
Figure 11. Within-event residuals of PGA from recorded ground motions relative to predictions of the NGA2, NGA2-I and Bea11 GMMs. Binned means shown with +/- one standard deviation.
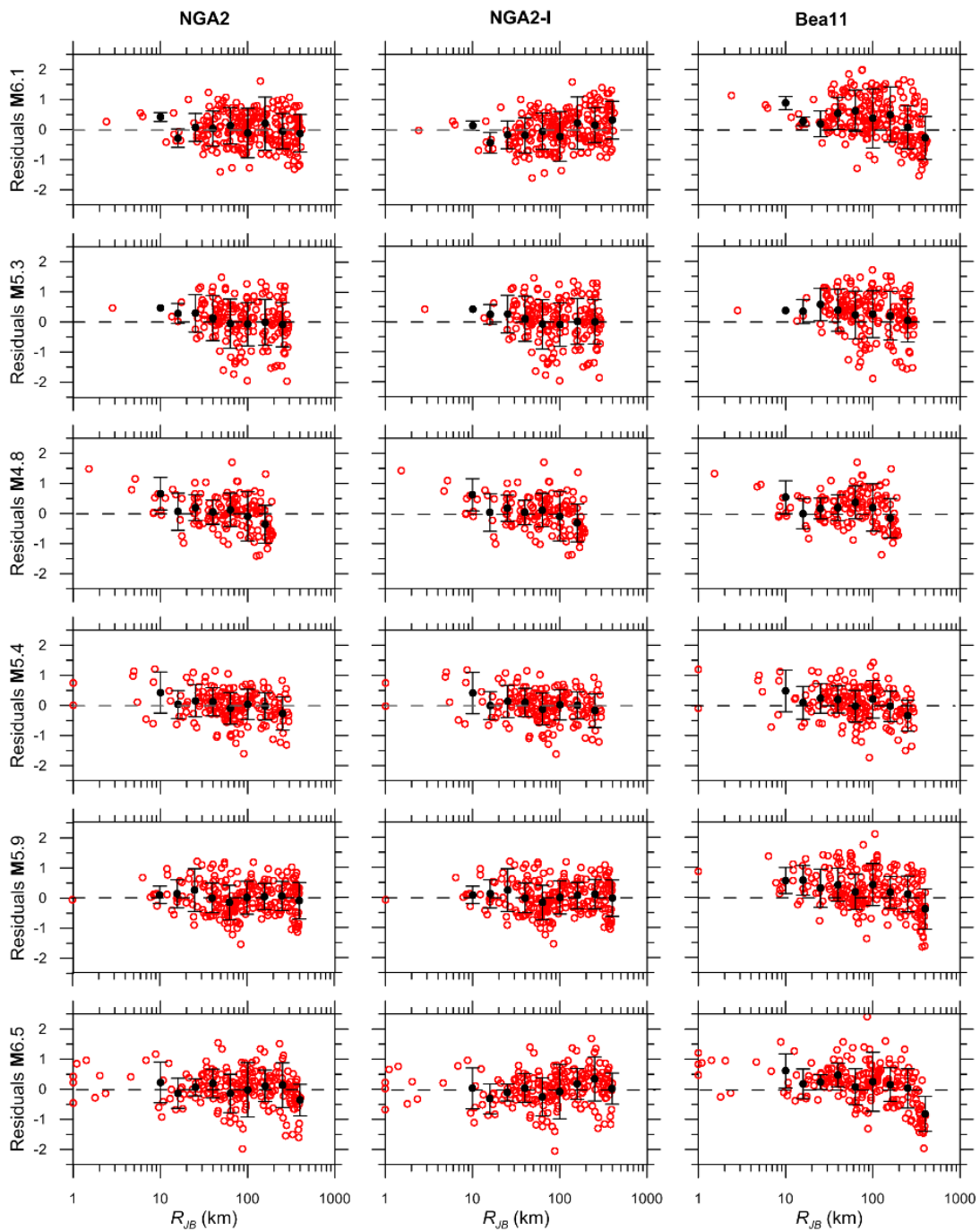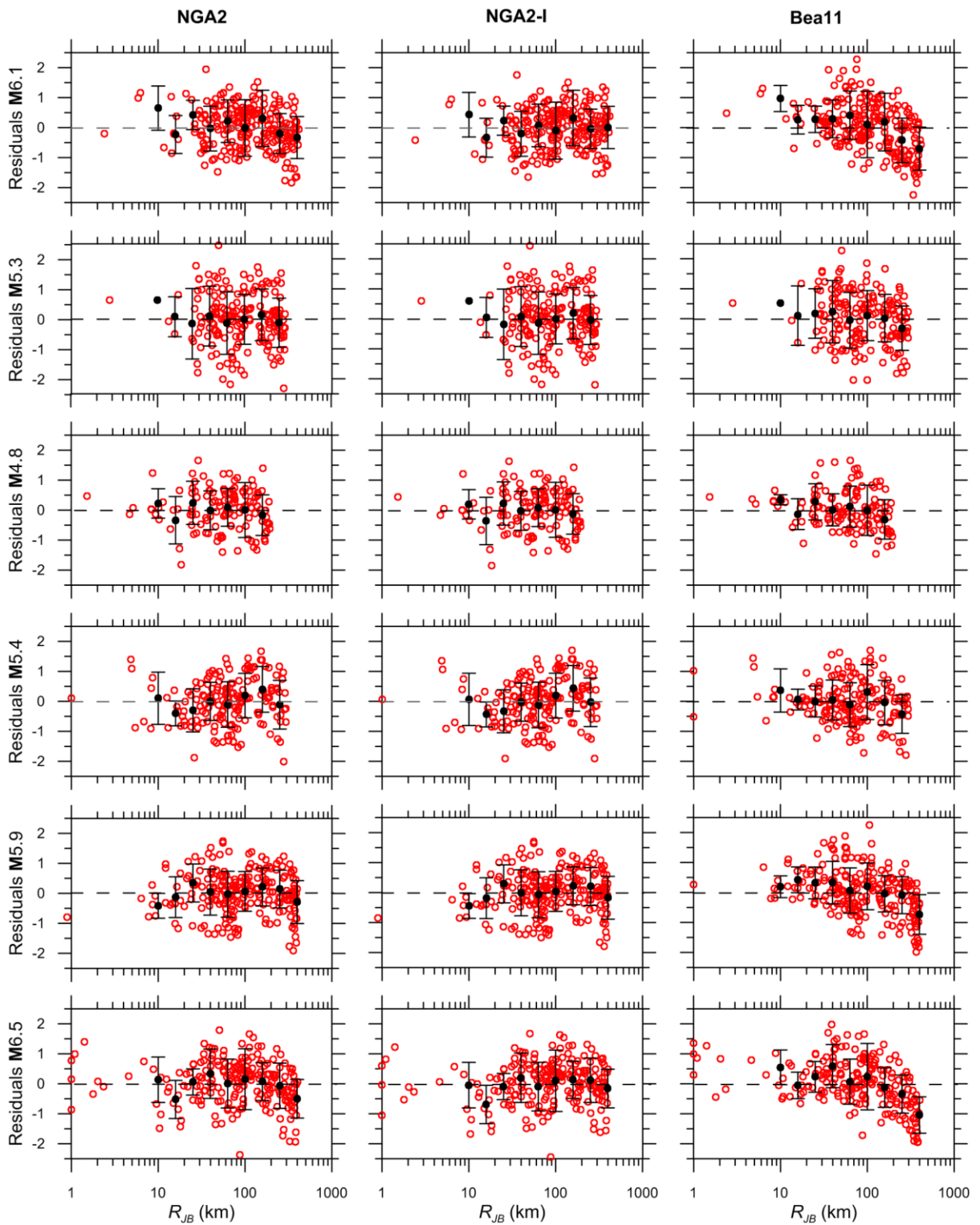
Figure 12. Within-event residuals of PGV from recorded ground motions relative to predictions of the NGA2, NGA2-I and Bea11 GMMs. Binned means shown with +/- one standard deviation.

Figure 13. Within-event residuals of PSA at 2 sec period from recorded ground motions relative to predictions of the NGA2, NGA2-I and Bea11 GMMs. Binned means shown with +/- one standard deviation.
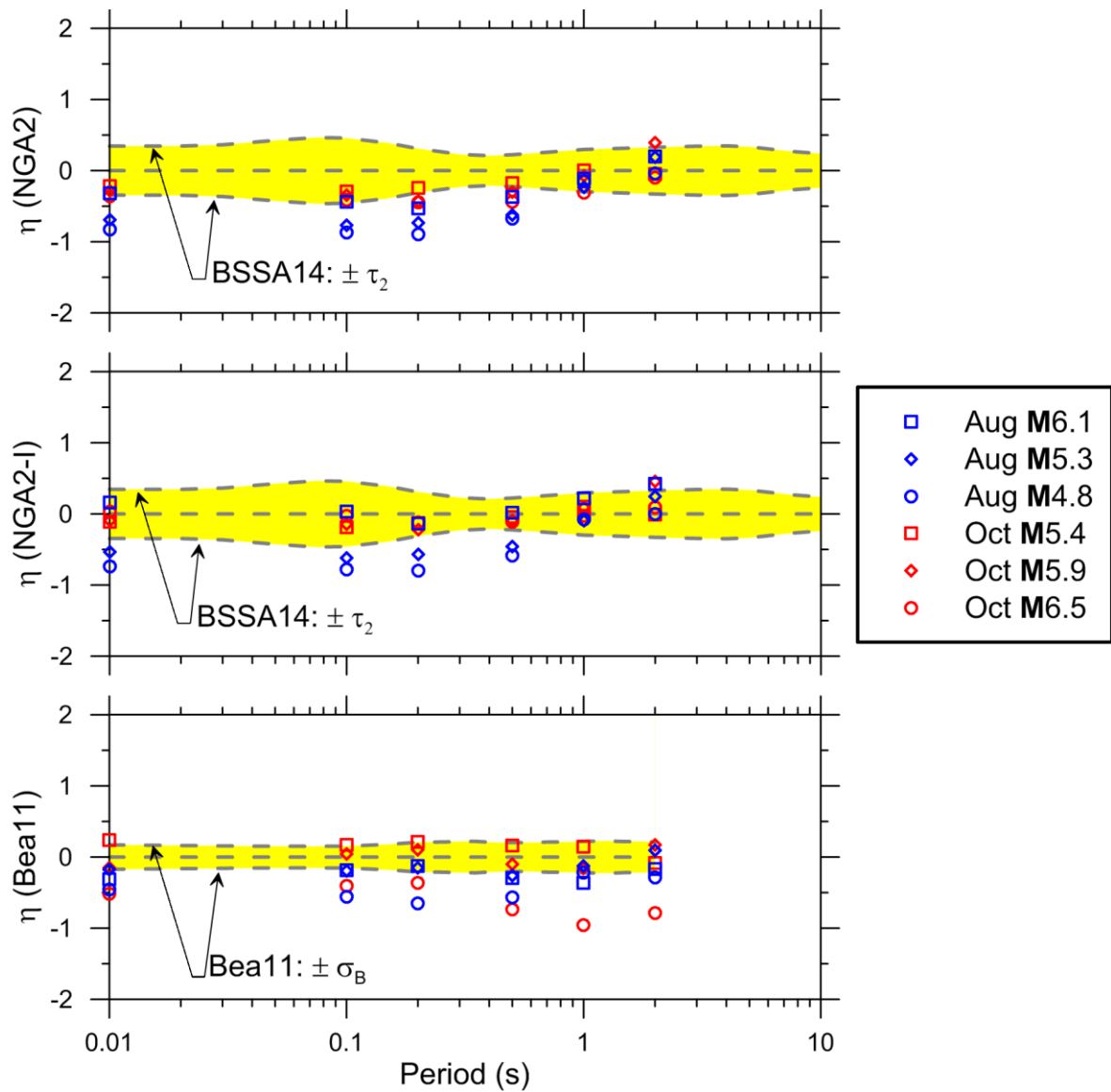
Figure 14. Event terms for PGA and PSA oscillator periods of 0.1-2.0 sec for the three sets of models and six events. For context, the +/- one between-event standard deviation is shown: τ_2 for **M**>5.5 from the Boore et al (2014) and σ_B from Bindi et al (2011).
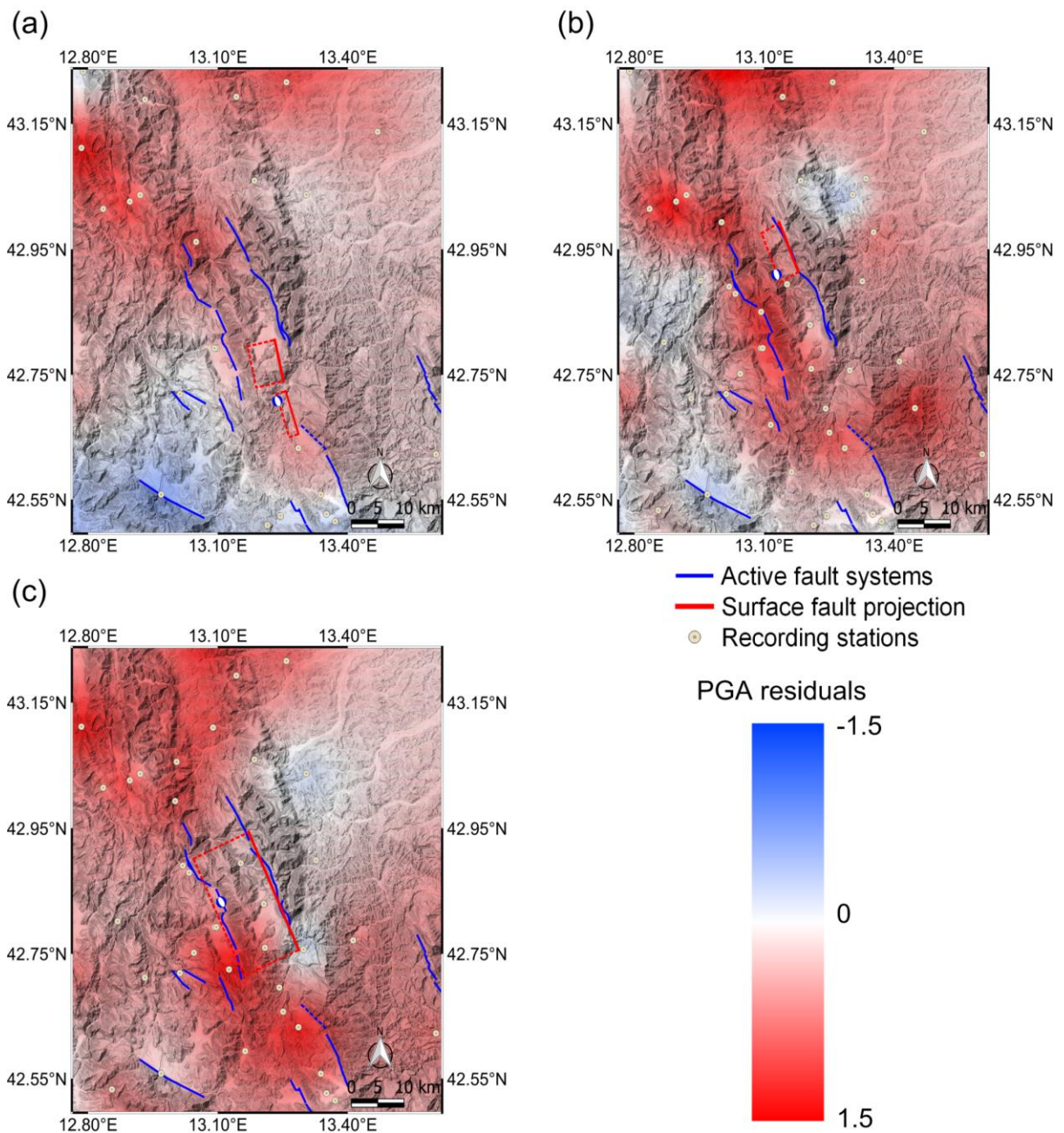
Figure 15. Map of the spatial distribution of PGA Residuals for: (a) **M**6.1 24 August, (b) **M**5.9 26 October, and (c) **M**6.5 30 October 2016 earthquakes.
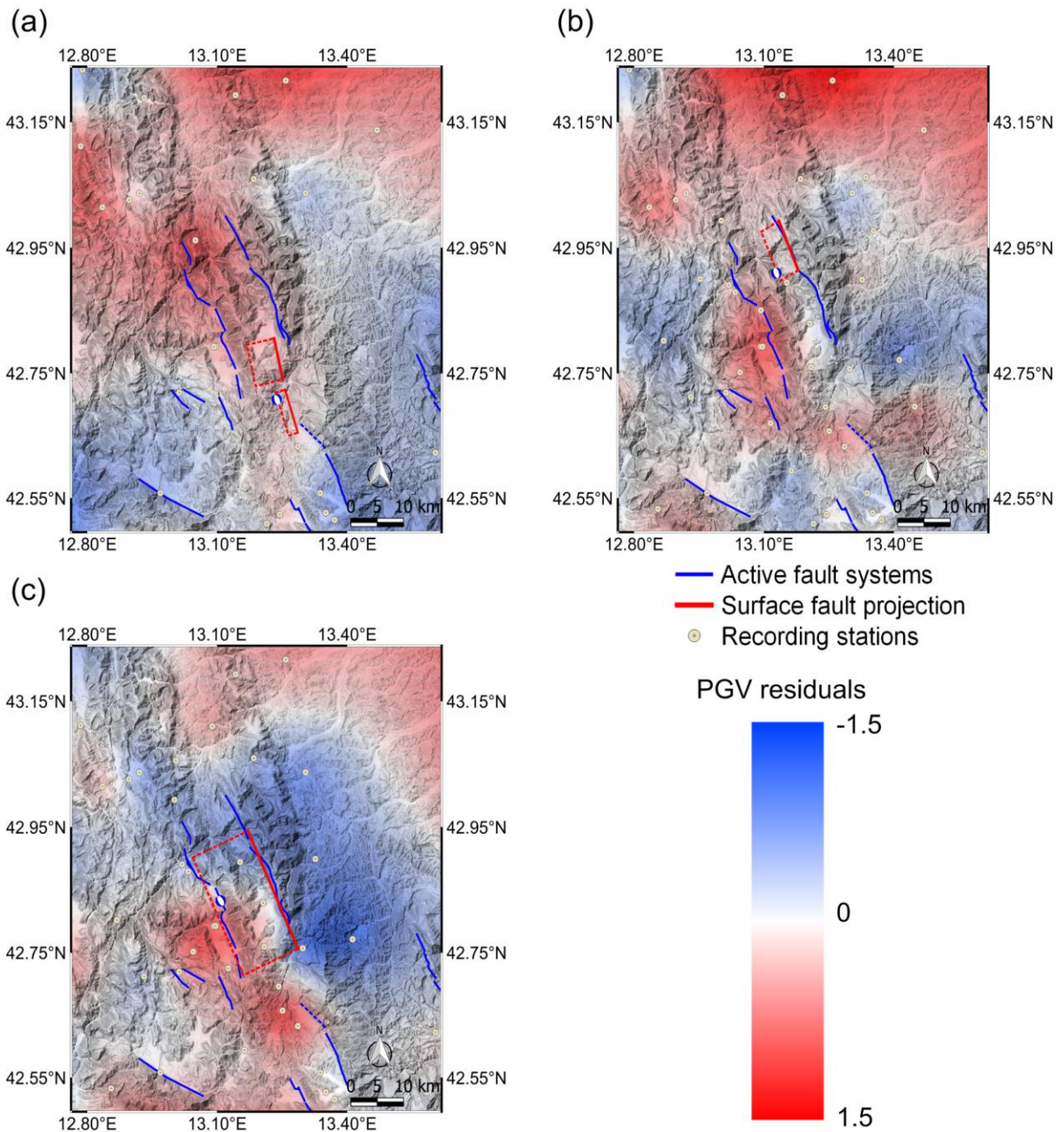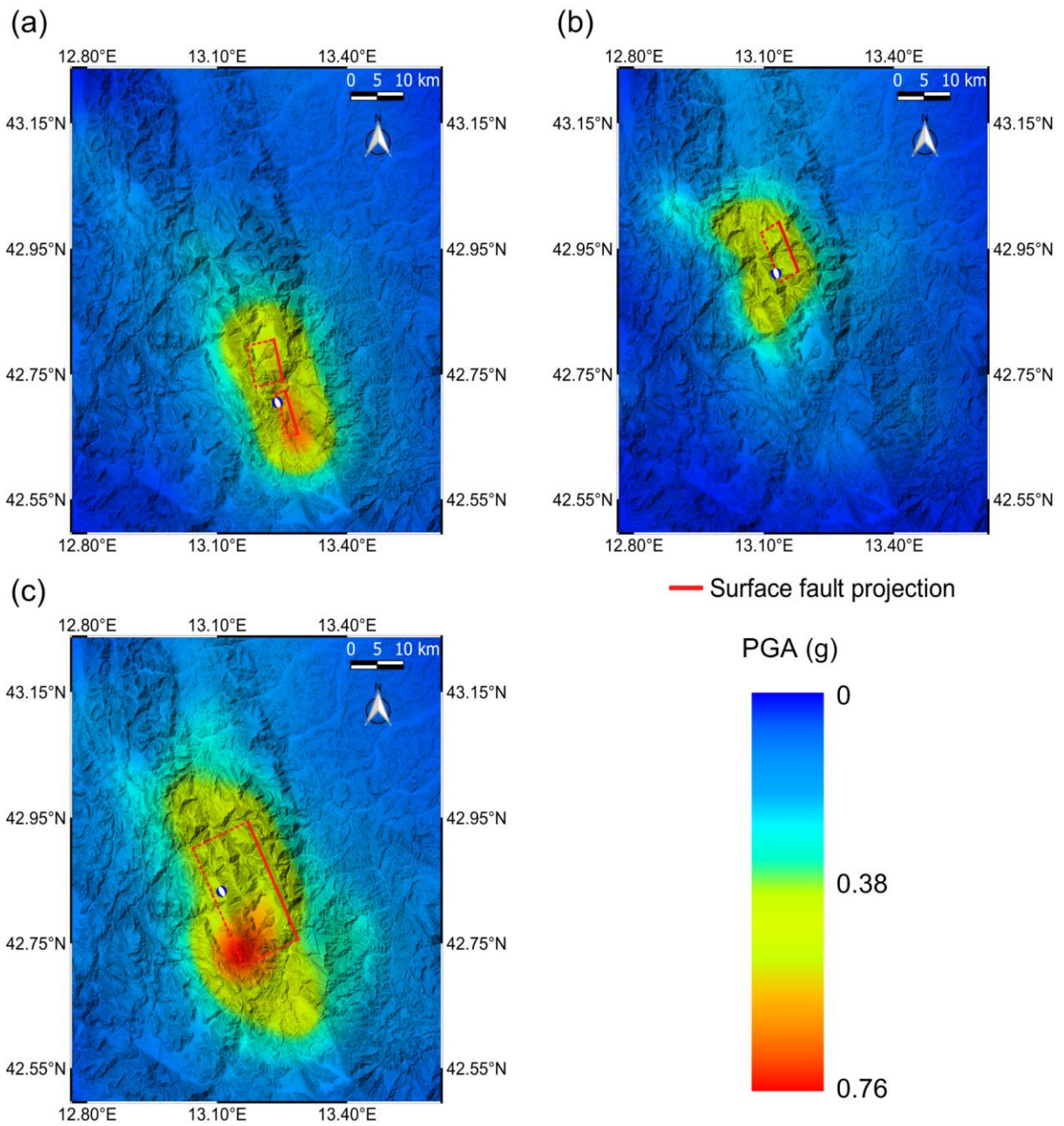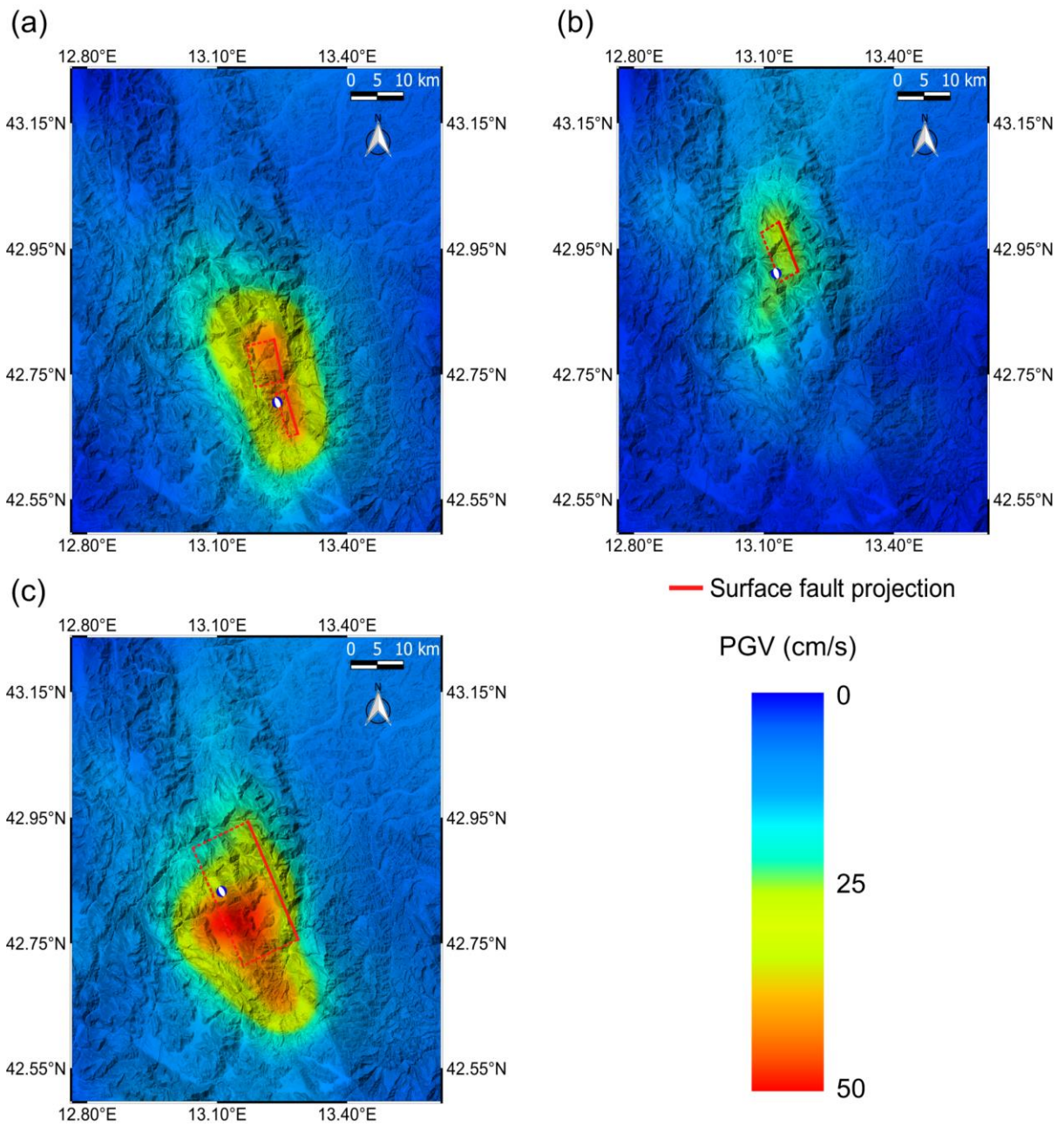
Figure 16. Map of the spatial distribution of PGV Residuals for: (a) **M**6.1 24 August, (b) **M**5.9 26 October, and (c) **M**6.5 30 October 2016 earthquakes.

Figure 17. Map of the spatial distribution of PGA for: (a) **M**6.1 24 August, (b) **M**5.9 26 October, and (c) **M**6.5 30 October 2016 earthquakes.

Figure 18. Map of the spatial distribution of PGV for: (a) **M**6.1 24 August, (b) **M**5.9 26 October, and (c) **M**6.5 30 October 2016 earthquakes.

SUMMARY AND CONCLUSIONS

The ground motions recorded during the 2016 Central Italy earthquake sequence are an invaluable resource for gaining improved understanding of seismic hazard associated with normal fault earthquakes, both as mainshock events and their aftershocks. Italy has several well-maintained networks of digital instruments that produced a rich inventory of data that will be studies for years to come. Our goals in this paper and related work (GEER 2016, 2017) were to provide a uniformly processed dataset, developed in a manner consistent with international standards, consisting of recordings and metadata for three notable mainshock events and three aftershocks.

All ground motions are uniformly processed on a component-by-component basis and produce lowest usable frequencies ranging from 0.02 to 3.6 Hz. Additional processing was performed of instruments in the near fault region to investigate fling step effects, and several instances of this are identified that produce displacements similar to those from adjacent GPS sensors. We examined the data for evidence of rupture directivity, but found neither consistent polarization of ground motion in the fault normal direction nor clear evidence of pulse-like features in velocity time series.

Source attributes are assigned to each recording using information from Galadini et al. (201x, this issue). Analysis of the data relative to ground motion models shows general under-prediction of near-fault ground motions, trends of scaling with distance that are general consistent with available models up to about 100 km, and relatively fast distance scaling beyond 100 km that is captured to a mixed degree by available models. We encourage the incorporation of these effects into future iterations of Italy-specific models.

Analysis of residuals indicates the ground motions from mainshock events are, on average, lower than expectation from global models at short periods. We also show regions around the faults with higher, and in a few cases, lower ground motions than expected based on Kriging of within-event residuals. These results are used to produce ground shaking maps applicable to a firm soil/weathered rock reference site condition.

ACKNOWLEDGEMENTS

REFERENCES

Abrahamson, N. A., Silva, W. J., and Kamai, R., 2014. Summary of the ASK14 ground motion relation for active crustal regions. *Earthquake Spectra*, **30**, 1025-1055.

Ancheta, T. D., Darragh, R. B., Stewart, J. P., Seyhan, E., Silva, W. J., Chiou, B. S. J., Wooddell, K. E., Graves, R. W., Kottke, A. R., Boore, D. M., Kishida, T., and Donahue, J. L., 2014. NGA-West2 database. *Earthquake Spectra*, **30**, 989–1005.

Baker, J.W., 2007. Quantitative classification of near-fault ground motions using wavelet analysis. *Bulletin of the Seismological Society of America*, **97**, 1486-1501.

Bindi, D., Pacor, F., Luzi, L., Puglia, R., Massa, M., Ameri, G., and Paolucci, R., 2011. Ground motion prediction equations derived from the Italian strong motion database. *Bulletin of Earthquake Engineering*, **9**, 1899-1920.

Boore, D. M., 2010. Orientation-independent, non geometric-mean measures of seismic intensity from two horizontal components of motion, *Bulletin of the Seismological Society of America*, **100**, 1830-1835.

Boore, D. M., and Kishida, T., 2017. Relations Between Some Horizontal-Component Ground-Motion Intensity Measures Used in Practice. *Bulletin of the Seismological Society of America*. **107**, 334-343.

Boore, D. M., Azari Sisi, A., and Akkar, S. (2012). Using Pad-Stripped Acausally Filtered Strong-Motion Data. *Bulletin of the Seismological Society of America*, **102**, 751–760.

Boore, D. M., Stewart, J. P., Seyhan, E., Atkinson, G. M., 2014. NGA-West 2 equations for predicting PGA, PGV, and 5%-damped PSA for shallow crustal earthquakes. *Earthquake Spectra*, **30**, 1057-1085.

Bozorgnia, Y., Abrahamson, N. A., Al Atik, L., Ancheta, T. D., Atkinson, G. M., Baker, J. W., Baltay,

72   A., Boore, D. M., Campbell, K. W., Chiou, B. S. J., Darragh, R. B., Day, S., Donahue, J. L., Graves,
73   R. W., Gregor, N., Hanks, T., Idriss, I. M., Kamai, R., Kishida, T., Kottke, A. R., Mahin, S. A.,
74   Rezaeian, S., Rowshandel, B., Seyhan, E., Shahi, S., Shantz, T., Silva, W. J., Spudich, P., Stewart,
75   J. P., Watson-Lamprey, J., Wooddell, K. E., and Youngs, R., 2014. NGA-West 2 research project.
76   *Earthquake Spectra*, **30**, 973-987.

77 Bradley, B. A., and Baker, J. W., 2015. Ground motion directionality in the 2010–2011 Canterbury
78   earthquakes, *Earthquake Engineering and Structural Dynamics*. **44**, 371–384.

79 Campbell, K. W., and Bozorgnia, Y., 2014. NGA-West2 ground motion model for the average
80   horizontal components of PGA, PGV, and 5% damped linear acceleration response spectra.
81   *Earthquake Spectra*, **30**, 1087-1115.

82 Chiaraluce, L., Di Stefano, R., Tinti, E., Scognamiglio, L., Michele, M., Casarotti, E., Cattaneo, M., De
83   Gori, P., Chiarabba, C., Monachesi, G., Lombardi, A., Valoroso, L., Latorre, D., and Marzorati, S.,
84   2017. The 2016 Central Italy seismic sequence: a first look at the mainshocks, aftershocks, and
85   source models. *Seismological Research Letters*, **88**, 757-771.

86 Chiou, B. S. J., and Youngs, R. R., 2014. Update of the Chiou and Youngs NGA model for the average
87   horizontal component of peak ground motion and response spectra. *Earthquake Spectra*, **30**, 1117-
88   1153.

89 d'Onofrio, A., Vitone, C., Cotecchia, F., Puglia, R., Santucci de Magistris, F., and Silvestri, F., 2009.
90   Caratterizzazione geotecnica del sottosuolo di San Giuliano di Puglia. *Rivista Italiana di*
91   *Geotecnica*, **3** (in Italian).

92 Delavaud, E., Cotton, F., Akkar, S., Scherbaum, F., Danciu, L., Beauval, C., Drouet, S., Douglas, J.,
93   Basili, R., Sandikkaya, M. A., Segou, M., Faccioli, E., and Theodoulidis, N., 2012. Toward a
94   ground-motion logic tree for probabilistic seismic hazard assessment in Europe. *Journal of*
95   *Seismology*, **16**, 451–473.

96 Durante, et al., 201x. Damage evaluation of roadway infrastructure during the 2016 Central Italy
97   earthquake sequence. *Earthquake Spectra*, in review.

98 Franke, et al., 201x. A multi-scale reconnaissance approach to documenting landslides following the
99   2016 Central Italy earthquakes. *Earthquake Spectra*, in review.

100 Galadini et al., 201x. Tectonic setting of 2016-2017 Central Italy event sequence and observed source
101   characteristics. *Earthquake Spectra*, in review.

102 Gardner, J. K., and Knopoff, L., 1974. Sequence of earthquakes in Southern-California, with
103   aftershocks removed, Poissonian? *Bulletin of the Seismological Society of America*, **64**, 1363-1367.

GEER, 2016. Engineering reconnaissance of the 24 August 2016 Central Italy Earthquake. Version 2, Zimmaro, P. and Stewart, J. P. (editors), Geotechnical Extreme Events Reconnaissance Association Report No. GEER-050B. doi: 10.18118/G61S3Z.

GEER, 2017. Engineering reconnaissance following the October 2016 Central Italy Earthquakes - Version 2, Zimmaro, P. and Stewart, J. P. (editors), Geotechnical Extreme Events Reconnaissance Association Report No. GEER-050D. doi: 10.18118/G6HS39.

Gregor, N., Silva, W. J., and Darragh R. B., 2002. Development of attenuation relations for peak particle velocity and displacement. A PEARL report to PG&E/CEC/Caltrans, June 12, 2002.

INGV working group, 2016. Secondo rapporto di sintesi sul Terremoto di Amatrice Ml 6.0 del 24 Agosto 2016 (Italia Centrale). doi: 10.5281/zenodo.154400 (in Italian).

Jayaram, N., and Baker, J. W., 2009. Correlation model for spatially distributed ground-motion intensities, *Earthquake Engineering and Structural Dynamics*, **38**, 1687–1708.

Kamai, R., Abrahamson, N.A., and Graves, R.W. 2014. Adding fling effects to processed ground-motion time histories, *Bull. Seism. Soc. Am.*, **104**, 1914-1929.

Kwak, D. Y., Mikami, A., Brandenberg, S. J., and Stewart, J. P., 2012. Ground motion estimation for evaluation of levee performance in past earthquakes. Proc. 9th International Conference on Urban Earthquake Engineering, 4th Asia Conference on Earthquake Engineering, Center for Urban Earthquake Engineering, March 6-8, 2012, Tokyo Institute of Technology, Tokyo, Japan.

Kwak, D. Y., Stewart, J. P., Brandenberg, S. J., and Mikami, A., 2016. Characterization of seismic levee fragility using field performance data, *Earthquake Spectra*, **32**, 193–215.

Luzi, L., Pacor, F., Puglia, R., Lanzano, G., Felicetta, C., D'Amico, M., Michelini, A., Faenza, L., Lauciani, V., Iervolino, I., Baltzopoulos, G., and Chioccarelli, E., 2017. The Central Italy seismic sequence between August and December 2016: analysis of strong-motion observations. *Seismological Research Letters,* **88**, 1219-1231.

Luzi, L., Puglia, R., Russo, E., ORFEUS WG5, 2016. Engineering strong motion database, version 1.0. Istituto Nazionale di Geofisica e Vulcanologia, Observatories & Research Facilities for European Seismology. doi: 10.13127/ESM.

Ministry of the Infrastructures - Italy, 2008. *Norme tecniche per le costruzioni*, Decree of the Minister of the Infrastructures, 14 January 2008, Gazzetta Ufficiale della Repubblica Italiana No. 29, Rome (in Italian).

Pacor, F., Paolucci, R., Ameri, G., Massa, M., Puglia, R., 2011. Italian strong motion records in ITACA: Overview and record processing, *Bulletin Earthquake Eng.*, **9**, 1741–1759.

Scasserra G., Stewart J. P., Kayen R. E., Lanzo G., 2009a. Database for earthquake strong motion studies in Italy. *Journal of Earthquake Engineering*, **13**, 852-881.

Scasserra, G, Stewart, J. P., Bazzurro, P., Lanzo, G., and Mollaioli, F., 2009b. A comparison of NGA ground-motion prediction equations to Italian data. *Bulletin of the Seismological Society of America*, **99**, 2961-2978.

Sextos, et al., 201x. Local patterns and incremental damage of buildings during the 2016 Central Italy earthquake sequence. *Earthquake Spectra*, in review.

Shahi, S. K., and Baker, J. W., 2014. An efficient algorithm to identify strong-velocity pulses in multicomponent ground motions. *Bulletin of the Seismological Society of America*, **104**, 2456-2466.

Somerville, P. G., Smith, N. F., Graves, R.W., and Abrahamson, N. N., 1997.Modification of empirical strong ground motion attenuation relations to include the amplitude and duration effects of rupture directivity, *Seismol. Res. Lett.,* **68**, 199–222.

Spudich, P., Bayless, J. R., Baker, J. W., Chiou, B. S., Rowshandel, B., Shahi, S. K., and Somerville P., 2013. *Final Report of the NGA-West2 Directivity Working Group*, PEER Report No. 2013/09, Pacific Earthquake Engineering Research Center, UC Berkeley, CA.

Stafford, P. J., 2012. Evaluation of structural performance in the immediate aftermath of an earthquake: a case study of the 2011 Christchurch earthquake, *International Journal of Forensic Engineering*, **1**, 58–77.

Stewart, J. P., Douglas, J., Javanbarg, M., Bozorgnia, Y., Abrahamson, N. A., Boore, D. M., Campbell, K. W., Delavaud, E., Erdik, M., and Stafford, P. J., 2015. Selection of ground motion prediction equations for the Global earthquake model. *Earthquake Spectra*, **31**, 19–45.

Stewart, J. P., Lanzo, G., Pagliaroli, A., Scasserra, G., Di Capua, G., Peppoloni, S., Darragh, R. B., and Gregor, M., 2012. Ground Motion Recordings from the Mw 6.3 2009 L'Aquila Earthquake in Italy and their Engineering Implications. *Earthquake Spectra*, **28**, 317-345.

Tinti, E., Scognamiglio, L., Michelini, A., and Cocco, M., 2016. Slip heterogeneity and directivity of the M_L 6.0, 2016, Amatrice earthquake estimated with rapid finite-fault inversion. *Geophysical Research Letters*, **43**, 10,745–10,752,

Wagener, T., Goda, K., Erdik, M., Daniell, J., and Wenzel, F., 2016. A spatial correlation model of peak ground acceleration and response spectra based on data of the Istanbul Earthquake Rapid Response and Early Warning System. *Soil Dynamics and Earthquake Engineering*, **85**, 166-178.

Watson-Lamprey, J., and Boore D.M., 2007. Beyond Sa_{GMRotI}: conversion to Sa_{Arb}, Sa_{SN}, and Sa_{MaxRot}, *Bulletin of the Seismological Society of America*, **97**, 1511-1524.

168   Wills, C. J., and Clahan, K. B., 2006. Developing a map of geologically defined site-condition
169   categories for California. *Bulletin of the Seismological Society of America*, **96**, 1483-1501.

170   Wooddell, K. E., and Abrahamson, N. A., 2014. Classification of main shocks and aftershocks in the
171   NGA-West2 database. *Earthquake Spectra*, **30**, 1257-1267.

172   Zimmaro, P., and Stewart, J. P., 2017. Site-specific seismic hazard analysis for Calabrian dam site using
173   regionally customized seismic source and ground motion models. *Soil Dynamics and Earthquake*
174   *Engineering*, **94**, 179-192.